11.1 EXPERIMENTS ON USING SCINTILLOMETERS TO INFER THE TURBULENT SURFACE FLUXES

Edgar L Andreas*
NorthWest Research Associates, Inc.; Lebanon, New Hampshire

1. INTRODUCTION

The scintillation of electromagnetic waves traveling through the atmospheric surface layer is presumed to provide information on the turbulent surface fluxes of momentum and sensible and latent heat. This idea goes back to at least Wesley (1976) and Wyngaard and Clifford (1978), and its implementation is another application of the so-called inertial-dissipation method (e.g., Taylor 1961; Fairall and Larsen 1986). Andreas (1990) reviews the theoretical and experimental foundation for this use of scintillometry.

Deriving the surface fluxes from scintillation measurements has presumed advantages over measuring the fluxes at a point with eddy-covariance instruments. Foremost is the notion that, because scintillation measurements yield path-averaged statistics, the derived fluxes might be representative area averages, even in nonhomogeneous terrain (Wyngaard and Clifford 1978; Coulter and Wesley 1980; Andreas 1989; Green et al. 1994; Beyrich et al. 2002). Such path-averaged fluxes could then provide appropriate validation data for remotely sensed fluxes and for weather forecast or general circulation models.

The scintillation method for obtaining the turbulent surface fluxes has been tested sporadically with various instrument configurations; validation has sometimes been promising (Hill et al. 1992; De Bruin et al. 1995; Green et al. 1997; Chehbouni et al. 1999), but few validation tests have used only path-averaging instruments to deduce the turbulent fluxes. In particular, the wind information needed to estimate the sensible and latent heat fluxes in other than free convection has often come from point instruments (e.g., Green et al. 1994; Kleissl et al. 2008). As a result, these tests produced no path-averaged measurement of the momentum flux.

The Scintec (Rottenburg, Germany) SLS20 surface-layer scintillometer system is designed to fill this need for path-averaged measurements of both the momentum and sensible heat fluxes (Thiermann 1992). The SLS20 is a displaced-beam scintillometer. The transmitter splits a single laser into two beams. The scintillation in either beam at the receiver gives the refractive index structure parameter, C_n^2. The correlation in intensity of the two beams at the receiver is a measure of the inner scale of turbulence, ℓ_0, which is, in turn, related to the dissipation rate of turbulent kinetic energy, ε. From C_n^2 and ε, we can iteratively solve equations based on Monin-Obukhov similarity theory for the surface stress or momentum flux, τ, and the sensible heat flux, H_s. Both are, thus, path-averaged estimates of these fluxes.

I used the Scintec SLS20 to measure τ and H_s in two experiments. One was the 1997–1998 experiment to study the Surface Heat Budget of the Arctic Ocean (SHEBA; Andreas et al. 1999; Uttal et al. 2002). The other was the 2005 Rapid Forcing Experiment (Andreas et al. 2006b, 2008a). Both experiments also included instruments near the scintillometer path that simultaneously measured τ and H_s by eddy-covariance. Here, I compare the scintillometer-derived H_s and τ (actually u_*, the friction velocity) with the eddy-covariance measurements of H_s and u_*.

I cannot conclude that the Scintec SLS20 made accurate measurements of u_* and H_s during these two diverse experiments. While the correlation between scintillometer H_s and eddy-covariance H_s was good in both experiments, the magnitude of the scintillometer H_s was biased low. When C_n^2 was at least $10^{-14}\,\mathrm{m}^{-2/3}$, the scintillometer u_* and the eddy-covariance u_* also had good correlation; the scintillometer u_*, though, was biased low. When C_n^2 was less than $10^{-14}\,\mathrm{m}^{-2/3}$, the correlation between scintillometer and eddy-covariance measurements of u_* was

*Corresponding author address: Dr. Edgar L Andreas, NorthWest Research Associates, Inc. (Seattle Division), 25 Eagle Ridge, Lebanon, NH 03766-1900; e-mail: eandreas@nwra.com.

only 0.33, and now the scintillometer u_* was biased high.

A key assumption for obtaining fluxes from scintillation data is that the path-averaged C_n^2 and ℓ_0 (or ε) obey Monin-Obukhov similarity theory. A related issue is what similarity functions to use for converting C_n^2 and ε to fluxes. Here, I have enough independent information to study what the Scintec SLS20 says about Monin-Obukhov similarity in both stable and unstable stratification. I use four distinct sets of functions for inferring u_* and H_s from scintillation data. None of these functions stand out, however, as the best set for obtaining fluxes from scintillation measurements.

When, alternatively, I determine the similarity functions for C_n^2 and ε from the scintillometer and eddy-covariance data, the derived values are so scattered that I cannot conclude that the path-averaged C_n^2 and ε, as measured by the Scintec SLS20, actually obey similarity theory. For example, the scintillometer-derived similarity function for ε is not one at neutral stratification, as required by similarity theory, but, rather, is about 0.3. That is, the scintillometer-based estimate of ε is biased very low. De Bruin et al. (2002) and Hartogensis et al. (2002) observed this same behavior in the SLS20.

2. MATHEMATICAL FRAMEWORK

In turbulence notation, my fluxes of interest are the surface momentum flux (or surface stress), τ, and the surface sensible heat flux, H_s:

$$\tau \equiv \rho u_*^2 = -\rho \overline{uw}, \qquad (2.1a)$$

$$H_s \equiv -\rho c_p u_* \theta_* = \rho c_p \overline{w\theta}. \qquad (2.1b)$$

Here, u and w are the turbulent fluctuations in the along-wind and vertical components of the wind vector, θ is the turbulent fluctuation in temperature, ρ is the air density, and c_p is the specific heat of air at constant pressure. The overbars indicate time averages. Equation (2.1a) also defines the friction velocity, u_*; and (2.1b) defines the temperature flux scale, θ_*. These two equations represent the so-called Reynolds fluxes measured by eddy-covariance instruments.

The fundamental measurements of the Scintec scintillometer are the refractive index structure parameter, C_n^2, and the inner scale of turbulence, ℓ_0. The inner scale is related to the dissipation rate of turbulent kinetic energy, ε, through (Hill and Clifford 1978; Andreas 1992; Hill 1997)

$$\ell_0 = \left[9\Gamma(1/3)\beta D\right]^{3/4} \varepsilon^{-1/4}. \qquad (2.2)$$

Here, Γ is the gamma function of the indicated argument (1/3); β is the one-dimensional Obukhov-Corrsin constant, about 0.40 (Andreas 1987; Sreenivasan 1996); and D is the thermal diffusivity of air.

The refractive index structure parameter is related to quantities with meteorological significance (e.g., Hill 1978; Andreas 1988):

$$C_n^2 = A^2 C_T^2 + 2ABC_{TQ} + B^2 C_Q^2. \qquad (2.3)$$

In this, C_T^2 is the temperature structure parameter; C_Q^2, the humidity structure parameter; and C_{TQ}, the temperature-humidity structure parameter. These are related to the spectra of temperature and humidity and to the temperature-humidity cospectrum and also to the surface fluxes of sensible and latent heat (e.g., Davidson et al. 1978; Fairall et al. 1980; Kohsiek 1982). The A and B in (2.3) are coefficients that depend on the wavelength λ of the electromagnetic wave and on mean pressure (P), temperature (T), and humidity (Q) (Andreas 1988).

For the wavelength of the Scintec SLS20, $\lambda = 0.685$ μm, C_n^2 depends only weakly on C_{TQ} and C_Q^2 (Andreas 1988), and I therefore ignore these terms in my analysis. That is,

$$C_n^2 = A^2 C_T^2, \qquad (2.4)$$

and (Andreas 1988)

$$A = -78.44\times10^{-6}\left(P/T^2\right). \qquad (2.5)$$

Here, A has units of K^{-1}, P must be in millibars, and T must be in kelvin (cf. Hill et al. 1992).

This C_T^2 is a variable that obeys Monin-Obukhov similarity theory (Wyngaard et al. 1971; Panofsky and Dutton 1984, p. 183; Hill 1989):

$$g(z/L) = \frac{z^{2/3} C_T^2}{\theta_*^2} = \frac{z^{2/3} C_n^2}{A^2 \theta_*^2}. \qquad (2.6)$$

Here, g is a presumed universal function of z, the height at which C_T^2 (or C_n^2) is measured, and L, the Obukhov length:

$$L^{-1} = \frac{\gamma k \theta_*}{T u_*^2}, \qquad (2.7)$$

where k (= 0.40) is the von Kármán constant and γ is the acceleration of gravity. The right-most term in (2.6) follows from (2.4).

The dissipation rate ε is likewise a similarity variable (e.g., Wyngaard and Coté 1971; Kaimal and Finnigan 1994, p. 16):

$$\phi_\varepsilon(z/L) = \frac{k z \varepsilon}{u_*^3}, \qquad (2.8)$$

where ϕ_ε is another presumed universal function of $\zeta \equiv z/L$.

With scintillometer measurements of C_n^2 and ℓ_0, the computational procedure is first to calculate ε from (2.2). Now iteratively solve the coupled equations (2.6)–(2.8) for u_*, θ_*, and L. The solution usually converges in five or six iterations. Finally, calculate τ and H_s from (2.1).

The crux of this analysis is specifying $g(\zeta)$ and $\phi_\varepsilon(\zeta)$.

3. SIMILARITY FUNCTIONS

Because the boundary-layer community has not converged on the best equations to use for $g(\zeta)$ and $\phi_\varepsilon(\zeta)$ when analyzing scintillometer data, I here try four distinct pairs of functions.

3.1 *Wyngaard*

Wyngaard et al. (1971) were the first to write expressions for $g(\zeta)$; Wyngaard (1973) offered slightly modified versions. Andreas (1988) further modified these functions for compatibility with a von Kármán constant of 0.40; Wyngaard et al. (1971) and Wyngaard (1973) had used 0.35 based on the Kansas data. The functions for $g(\zeta)$ that I will henceforth identify as the "Wyngaard" functions are, thus,

$$g(\zeta) = 4.9(1 - 6.1\zeta)^{-2/3} \quad \text{for } \zeta \le 0, \qquad (3.1a)$$

$$g(\zeta) = 4.9\left(1 + 2.2\zeta^{2/3}\right) \quad \text{for } \zeta \ge 0. \qquad (3.1b)$$

During this same period, Wyngaard and Coté (1971) were the first to derive expressions for $\phi_\varepsilon(\zeta)$. Again, Andreas (1988) modified these to reflect a von Kármán constant of 0.40:

$$\phi_\varepsilon(\zeta) = \left[1 + 0.46(-\zeta)^{2/3}\right]^{3/2} \quad \text{for } \zeta \le 0, \qquad (3.2a)$$

$$\phi_\varepsilon(\zeta) = \left[1 + 2.3\zeta^{3/5}\right]^{3/2} \quad \text{for } \zeta \ge 0. \qquad (3.2b)$$

I will refer to these as the "Wyngaard" functions for ϕ_ε.

3.2 *Thiermann-Grassl*

Thiermann and Grassl (1992) developed the first set of similarity functions specifically for obtaining the surface fluxes from scintillometer measurements of C_n^2 and ℓ_0. I will henceforth refer to these as the "Thiermann-Grassl" functions:

$$g(\zeta) = 6.34\left(1 - 7\zeta + 75\zeta^2\right)^{-1/3} \quad \text{for } \zeta \le 0, \qquad (3.3a)$$

$$g(\zeta) = 6.34\left(1 + 7\zeta + 20\zeta^2\right)^{1/3} \quad \text{for } \zeta \ge 0, \qquad (3.3b)$$

and

$$\phi_\varepsilon(\zeta) = (1 - 3\zeta)^{-1} - \zeta \quad \text{for } \zeta \le 0, \qquad (3.4a)$$

$$\phi_\varepsilon(\zeta) = \left(1 + 4\zeta + 16\zeta^2\right)^{1/2} \quad \text{for } \zeta \ge 0. \qquad (3.4b)$$

Equations (3.3) are slightly different than what Thiermann and Grassl (1992) gave. Their definition of $g(\zeta)$ was unusual in that it had the von Kármán constant multiplying z [cf. (2.6)]. I removed this k and modified their given similarity functions accordingly to obtain (3.3).

3.3 *Edson-Fairall*

From eddy-covariance measurements over the ocean, Edson and Fairall (1998) deduced the following similarity functions:

$$g(\zeta) = 5.9(1 - 8\zeta)^{-2/3} \quad \text{for } \zeta \le 0, \qquad (3.5a)$$

$$g(\zeta) = \frac{5.9(1 + 6\zeta)}{(1 + 5\zeta)^{1/3}} \quad \text{for } \zeta \ge 0, \qquad (3.5b)$$

and

$$\phi_\varepsilon(\zeta) = \frac{1-\zeta}{1-7\zeta} - \zeta \quad \text{for} \quad \zeta \le 0, \qquad (3.6a)$$

$$\phi_\varepsilon(\zeta) = 1 + 5\zeta \quad \text{for} \quad \zeta \ge 0. \qquad (3.6b)$$

I will refer to these as the "Edson-Fairall" functions.

3.4 *Budget method*

In steady-state, the budget equation for temperature variance in the atmospheric surface layer simplifies to a balance between production and dissipation (e.g., Large and Pond 1982; Panofsky and Dutton 1984, p. 94, 184; Andreas 1987):

$$2u_*\theta_*\frac{\partial\Theta}{\partial z} = N_\theta. \qquad (3.7)$$

In this, N_θ is the dissipation rate of temperature variance, and Θ is the average potential temperature; thus, $\partial\Theta/\partial z$ is the vertical gradient in potential temperature. The left term is the production of temperature variance; the right term, the dissipation of it.

The Monin-Obukhov similarity function for the nondimensional temperature gradient is

$$\phi_h(\zeta) = \frac{kz}{\theta_*}\frac{\partial\Theta}{\partial z}. \qquad (3.8)$$

The dissipation rate of temperature variance is also related to C_T^2 through the temperature spectrum in the inertial-convective subrange such that (Hill and Clifford 1978; Andreas 1988)

$$\beta N_\theta \varepsilon^{-1/3} = 0.249 C_T^2. \qquad (3.9)$$

On inserting (3.8) and (3.9) into (3.7) and using the definition of ϕ_ε, (2.8), we obtain (Andreas 1988; cf. Panofsky and Dutton 1984, p. 184)

$$\frac{2\beta\phi_h(\zeta)}{0.249k^{2/3}\phi_\varepsilon(\zeta)^{1/3}} = \frac{z^{2/3}C_T^2}{\theta_*^2} \equiv g(\zeta). \qquad (3.10)$$

That is, the temperature variance budget also yields an expression for $g(\zeta)$.

Equation (3.10) has two advantages over my earlier expressions for $g(\zeta)$. Notice that (3.1), (3.3), and (3.5) offer several opinions as to the value of $g(\zeta)$ at neutral stratification. Equation (3.10) provides a theoretical expression for that coefficient. On evaluating the constants on the left side of (3.10), I get

$$g(\zeta) = \frac{5.92\phi_h(\zeta)}{\phi_\varepsilon(\zeta)^{1/3}}; \qquad (3.11)$$

$g(\zeta)$ is thus predicted to be 5.92 at neutral stratification.

The second advantage of (3.10) is that I can use functions of my own choosing for ϕ_h and ϕ_ε. For compatibility with other of my algorithms (i.e., Andreas et al. 2008b, 2010a, 2010b), I use the function from Paulson (1970) for ϕ_h in unstable stratification,

$$\phi_h(\zeta) = (1-16\zeta)^{-1/2}, \qquad (3.12a)$$

and the new function from Grachev et al. (2007) in stable stratification,

$$\phi_h(\zeta) = 1 + \frac{5\zeta + 5\zeta^2}{1 + 3\zeta + \zeta^2}. \qquad (3.12b)$$

For ϕ_ε in (3.11), I use the functions that I derive next from the turbulent kinetic energy equation.

Again, in steady-state, the turbulent kinetic energy equation also reflects a near-balance between production and dissipation (Large and Pond 1981; Panofsky and Dutton 1984, p. 93f.; Wyngaard 2010, p. 231):

$$u_*^2\frac{\partial U}{\partial z} - \frac{\gamma}{T}u_*\theta_* = \varepsilon. \qquad (3.13)$$

Here, U is the mean wind speed; thus, $\partial U/\partial z$ is the vertical gradient in wind speed. As with (3.7), the terms on the left are the surface-layer production of turbulent kinetic energy; the term on the right is the dissipation.

On introducing the nondimensional gradient in wind speed,

$$\phi_m(\zeta) = \frac{kz}{u_*}\frac{\partial U}{\partial z}, \qquad (3.14)$$

and using (2.7) and (2.8), we can rewrite (3.13) as

$$\phi_m(\zeta) - \zeta = \phi_\varepsilon(\zeta). \qquad (3.15)$$

This is a budget-based expression for ϕ_ε. For consistency in my terminology, I use this expression for ϕ_ε in my budget-based expression for $g(\zeta)$, (3.11).

As with (3.11), I now have the option of choosing ϕ_m for compatibility with my other algorithms. Hence, for ϕ_m in unstable stratification, I use the function from Paulson (1970):

$$\phi_m(\zeta) = (1 - 16\zeta)^{-1/4}. \qquad (3.16a)$$

In stable stratification, I use the new result from Grachev et al. (2007):

$$\phi_m(\zeta) = 1 + \frac{6.5\zeta(1+\zeta)^{1/3}}{1.3 + \zeta}. \qquad (3.16b)$$

Another advantage of these budget results, (3.11) and (3.15), is that they provide a way to incorporate into $g(\zeta)$ and $\phi_\varepsilon(\zeta)$ new similarity functions to treat the very stable stratification that we saw over sea ice—namely, those from Grachev et al. (2007).

3.5 *System of Equations*

In summary, three coupled equations are necessary for estimating u_* and H_s $(=-\rho c_p u_* \theta_*)$ from scintillometer measurements of C_n^2 and ℓ_0. Once ℓ_0 is converted to ε through (2.2), the three coupled equations derive from (2.6), (2.7), and (2.8):

$$\theta_* = \left[\frac{z^{2/3} C_n^2}{A^2 g(\zeta)}\right]^{1/2}, \qquad (3.17a)$$

$$u_* = \left[\frac{k z \varepsilon}{\phi_\varepsilon(\zeta)}\right]^{1/3}, \qquad (3.17b)$$

$$\zeta = \frac{z}{L} = \frac{\gamma k z \theta_*}{T u_*^2}. \qquad (3.17c)$$

Here, z is the path height of the scintillometer beam. Clearly, we also need average pressure and temperature for calculating A and ζ.

Notice the square root in (3.17a): Scintillometer data do not tell us the sign of the sensible heat flux or the sign of the stratification. For my analysis here, I chose the sign of the scintillometer-derived H_s to agree with the sign of the eddy-covariance H_s. In later scatter plots, this choice (perhaps artificially) improves the apparent correlation between scintillometer and eddy-covariance sensible heat fluxes because the fluxes are always in the first or third quadrants.

With the four sets of $g(\zeta)$ and $\phi_\varepsilon(\zeta)$ functions, I invoke (3.17) four times for each set of C_n^2 and ℓ_0 measurements and analyze all the resulting flux estimates.

4. DATASETS

4.1 *The Two Sites*

The Scintec scintillometer that we used during SHEBA and the Rapid Forcing Experiment was an upgraded version of the standard SLS20 for use over longer propagation paths. It thus had a slightly more powerful laser that operated at a wavelength of 0.685 μm instead of the 0.670-μm wavelength of the standard SLS20.

During the year-long SHEBA experiment, the scintillometer was placed on multiyear Arctic sea ice (Andreas et al. 1999, 2003). Because of instrument problems, the scintillometer did not run continuously as the other SHEBA instruments did. We have "winter" data from 31 October to 2 December 1997 and "summer" data from 20 May to 2 June 1998. During the winter measurements, the propagation path was 350 m at a height of 2.88 m. During summer, the propagation path was 300 m at a height of 2.60 m

The SHEBA site was nearly ideal for a micrometeorological study. The surface was snow-covered sea ice in all directions for hundreds of kilometers. The ice itself was ridged, as is typical of Arctic sea ice. These ridges affected the aerodynamic roughness of the surface but were randomly distributed and, thus, did not alter the overall horizontal homogeneity of the surface. Occasional leads broke the sea ice to expose warm water, but none opened in the immediate vicinity of the scintillometer. Because sea ice is horizontal, the SHEBA site was unaffected by density currents that are outside the scope of Monin-Obukhov similarity theory.

The site for the Rapid Forcing Experiment, in contrast, was not as ideal. That experiment took place in a 15-acre field in rural Lebanon, New Hampshire (Andreas et al. 2006b, 2008a). The field had 5–10-m trees to the west and north and was sloping—about 6% from east to west. The

scintillometer path and the eddy-covariance instruments were set up to take best advantage of the dominant wind direction, which was westerly and northwesterly. The 182-m scintillometer propagation path ran south-southeasterly from the transmitter to the receiver at a height of 2.44 m. This set-up gave a couple hundred meters of fetch over the field to the scintillometer path and to the point instruments.

The experiment ran from 11 to 27 April 2005. The field had been mowed the previous autumn. The experiment thus began with the field covered in grass stubble and clippings a few tens of millimeters thick; the grass was dormant, and the ground was near freezing. The ground warmed and the grass greened up by the end of the experiment but was still short.

Because the Rapid Forcing site was not ideal, its data provide an opportunity to evaluate the notion that scintillometer-derived fluxes are representative values even in complex terrain.

4.2 *Scintillometer Data*

The fundamental data that the Scintec SLS20 yields are minute averages of C_n^2, ℓ_0, and a data-quality number designated NOK. To obtain these averages, the system software divides each minute into ten 6-second blocks. For the first block of each minute, the software turns off the laser and measures the background. This background calibration is applied to the nine subsequent blocks for that minute. Each of these nine blocks yields a measurements of C_n^2 and ℓ_0; the software also evaluates the quality of each data block. If the block passes the quality control criteria, its C_n^2 and ℓ_0 values are used for computing the minute averages; otherwise, the block is ignored. NOK reports how many of the nine available data blocks are used in finding the minute averages of C_n^2 and ℓ_0.

For both the SHEBA and Rapid Forcing experiments, I further averaged these minute data into hourly values to coincide with the simultaneous hourly averages from the eddy-covariance instruments. I weighted each minute average of C_n^2 and ℓ_0 in these hourly averages according to NOK and further used NOK to calculate a "quality" for the hourly averages (same for both C_n^2 and ℓ_0). Essentially, this quality metric reflects the percentage of good measurements during the hour. In my analysis here, I ignored any hourly scintillometer data for which the computed quality metric was less than 25%. These were cases in which fewer than 25% of the scintillometer measurements during an hour passed quality controls.

4.3 *Eddy-Covariance Data*

My purpose in this paper is to compare the hourly scintillometer-derived estimates of u_* and H_s with simultaneous eddy-covariance measurements of these quantities. Both the SHEBA and Rapid Forcing experiments included eddy-covariance measurement of u_* and H_s [see (2.1)] with sonic anemometers made by Applied Technologies Inc. (ATI; Kaimal et al. 1990; Kaimal and Gaynor 1991; Kaimal and Finnigan 1994, p. 218f.). These sonics sampled at 10 Hz. For SHEBA, a 20-m tower with ATI sonics at five levels was near the receiver end of the scintillometer path. The Rapid Forcing Experiment had a single sonic positioned near the center of the scintillometer path at a height of 3.6 m.

Persson et al. (2002), Grachev et al. (2005, 2007), and Andreas et al. (2006a, 2010a, 2010b) provide many more details of the SHEBA eddy-covariance measurements. The only point I need to make is that the SHEBA tower yielded up to five independent measurements of u_* and H_s each hour. As the SHEBA eddy-covariance values of u_* and H_s for the subsequent comparisons, I use the median values of all reported hourly u_* and H_s measurements.

Similarly, Andreas et al. (2006b, 2008a) provide details on the point turbulence measurements during the Rapid Forcing Experiment and on how we computed the hourly averaged values of u_* and H_s. Briefly, because these measurements were on a slope, we could not base coordinate rotations on the assumption that the average vertical velocity was zero. Rather, we assumed that the sonic anemometer was properly leveled and, thus, made only one coordinate rotation—aligning $\overline{uw}$ with the mean wind direction.

5. FLUX COMPARISONS

5.1 *SHEBA*

About half of the SHEBA scintillometer data had C_n^2 values less than $10^{-14}\,\mathrm{m}^{-2/3}$. The scatter

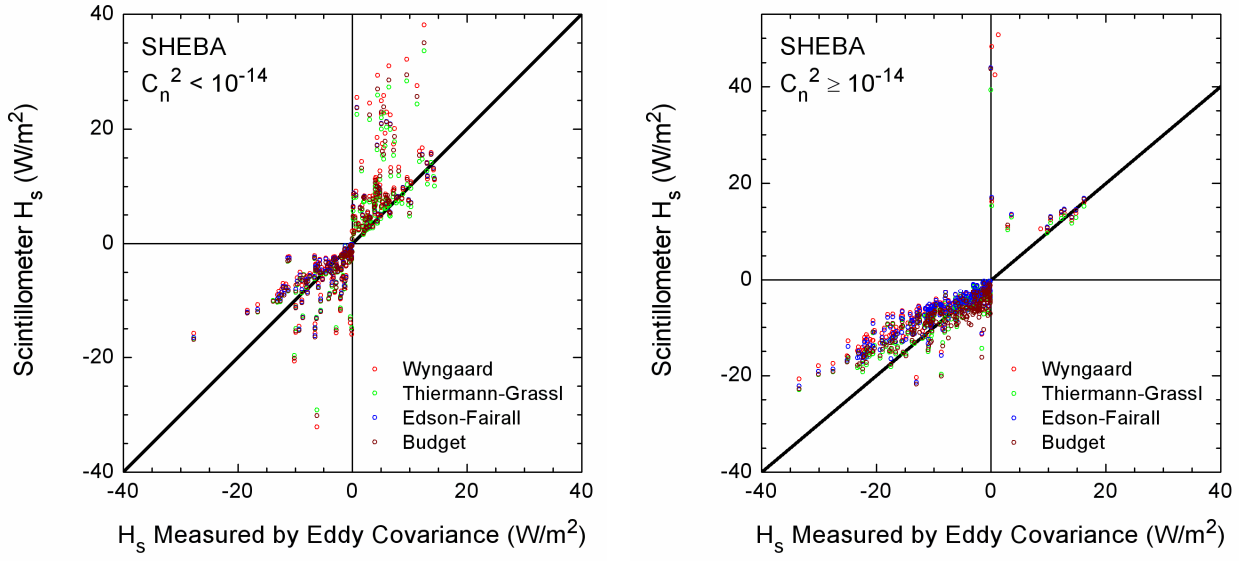

FIG. 1 The hourly SHEBA scintillometer measurements of sensible heat flux, H_s, are compared with simultaneous eddy-covariance measurements of H_s. The panels show cases when $C_n^2 < 10^{-14}\,\mathrm{m}^{-2/3}$ and when $C_n^2 \geq 10^{-14}\,\mathrm{m}^{-2/3}$. Four different sets of similarity functions, as described in Section 3.1–3.4, are used for evaluating the scintillometer H_s. The heavy line is 1:1.

plots of scintillometer versus eddy-covariance data for both u_* and H_s had different characteristics when C_n^2 was less than $10^{-14}\,\mathrm{m}^{-2/3}$ and when C_n^2 was above this value. Figures 1 and 2 thus show the H_s and u_* scatter plots for the two C_n^2 ranges individually.

A key feature of the sensible heat flux plots is how small the fluxes are: $|H_s|$ is rarely larger than 20 W m^{-2}. Such small fluxes are typical over sea ice (Persson et al. 2002; Andreas et al. 2010a,

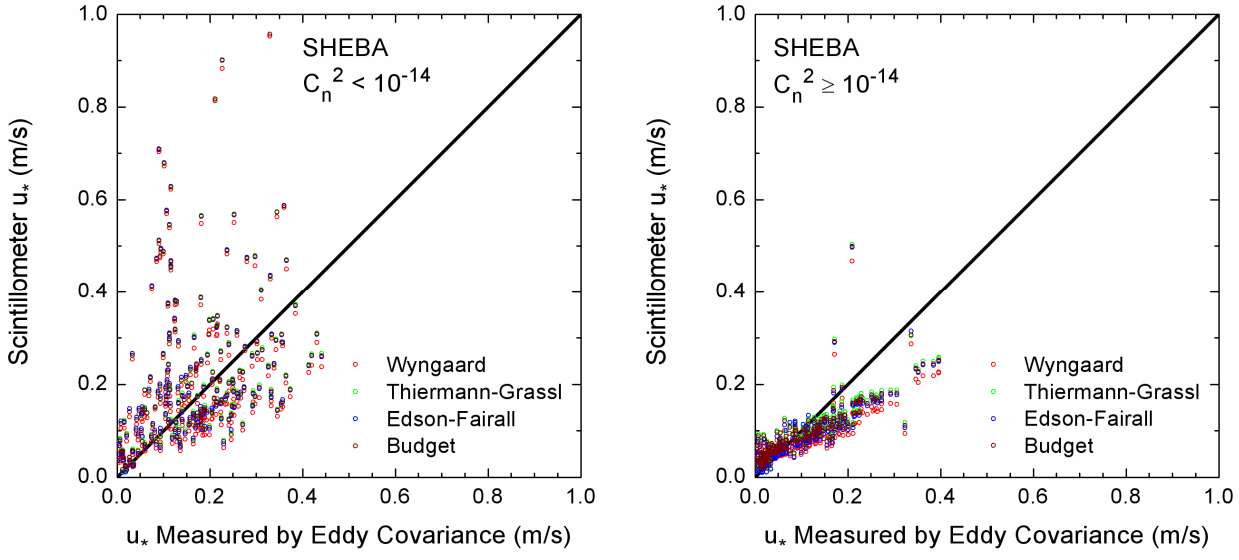

FIG. 2. As in Fig. 1, except these are scatter plots for the friction velocity, u_*.

TABLE 1. The correlation coefficient, the mean bias error (MBE), and the root-mean-square error (RMSE) for comparisons of scintillometer-derived and eddy-covariance sensible heat flux (H_s) and friction velocity (u_*) for the SHEBA data. The scintillometer-derived values are based on the four sets of similarity functions described in Section 3; "Number" is the number of data pairs in a given category. As explained in the text, I made these comparisons for cases with $C_n^2 < 10^{-14}\,\mathrm{m}^{-2/3}$ and with $C_n^2 \geq 10^{-14}\,\mathrm{m}^{-2/3}$.

	Wyngaard	Thiermann-Grassl	Edson-Fairall	Budget
H_s Comparison				
$C_n^2 < 10^{-14}\,\mathrm{m}^{-2/3}$				
Number	234	233	233	233
Correl. Coef.	0.777	0.799	0.797	0.801
MBE (W m^{-2})	1.79	1.10	1.51	1.38
RMSE (W m^{-2})	6.72	5.87	6.21	6.20
$C_n^2 \geq 10^{-14}\,\mathrm{m}^{-2/3}$				
Number	253	249	249	248
Correl. Coef.	0.657	0.813	0.790	0.764
MBE (W m^{-2})	2.65	0.76	1.98	0.14
RMSE (W m^{-2})	7.52	4.76	5.33	5.26
u_* Comparison				
$C_n^2 < 10^{-14}\,\mathrm{m}^{-2/3}$				
Number	221	220	220	220
Correl. Coef.	0.325	0.341	0.335	0.337
MBE (m s^{-1})	0.036	0.049	0.048	0.048
RMSE (m s^{-1})	0.162	0.163	0.164	0.164
$C_n^2 \geq 10^{-14}\,\mathrm{m}^{-2/3}$				
Number	226	223	223	223
Correl. Coef.	0.820	0.845	0.833	0.833
MBE (m s^{-1})	-0.029	-0.013	-0.021	-0.014
RMSE (m s^{-1})	0.061	0.051	0.055	0.053

2010b) and explain why C_n^2 was often so small.

In Figs. 1 and 2, the H_s and u_* pairs with $C_n^2 < 10^{-14}\,\mathrm{m}^{-2/3}$ are more scattered than the pairs for which $C_n^2 \geq 10^{-14}\,\mathrm{m}^{-2/3}$. I presume that the signal-to-noise ratio of the scintillometer is less when $C_n^2 < 10^{-14}\,\mathrm{m}^{-2/3}$; consequently, both C_n^2 and ℓ_0 are not measured as precisely as when $C_n^2 \geq 10^{-14}\,\mathrm{m}^{-2/3}$.

Neither Figs. 1 nor 2 provides obvious guidance for choosing among the four sets of similarity functions. In the sensible heat flux panels (Fig. 1), the Wyngaard functions stand out as giving larger fluxes than the other functions. In the friction velocity panels (Fig. 2), the Wyngaard functions tend to produce lower u_* than the other functions.

To quantify the performance of the various similarity functions, I computed the mean bias error (MBE) and the root-mean-square error (RMSE) (Willmott 1982) for the scintillometer-derived fluxes. Let S_i be an hourly scintillometer-derived flux (either H_s or u_*), and let M_i be the corresponding eddy-covariance value. Then,

$$\mathrm{MBE} = \frac{1}{N}\sum_{i=1}^{N}(S_i - M_i), \qquad (5.1)$$

$$\mathrm{RMSE} = \left[\frac{1}{N}\sum_{i=1}^{N}(S_i - M_i)^2\right]^{1/2}, \qquad (5.2)$$

where N is the number of data pairs.

Table 1 shows these overall metrics for the

scatter plots in Figs. 1 and 2. Table 1 also lists the correlation coefficient for each panel and for each set of similarity functions.

Lastly, the table lists the number of data pairs. These numbers are not all the same because, sometimes, the scintillometer iteration did not converge. If my analysis routine made 20 iterations without u_* and θ_* converging to within 0.1%, I assumed that the iteration failed. The Wyngaard equations were better at providing solutions than were the other similarity functions. Most of the failures to converge occurred in unstable stratification. Most of the failures in the Thiermann-Grassl, Edson-Fairall, and Budget functions were for the same C_n^2 and ℓ_0 pairs.

Table 1 quantifies some of the visual observations we made. The Wyngaard functions produce the largest MBE and RMSE for the sensible heat flux data. The Thiermann-Grassl and Budget functions do best for predicting sensible heat flux. The Thiermann-Grassl functions always give the smallest RMSE; but the Budget functions yield a very small MBE when $C_n^2 \geq 10^{-14}\,\mathrm{m}^{-2/3}$.

The u_* metrics in Table 1 are much better for the cases when $C_n^2 \geq 10^{-14}\,\mathrm{m}^{-2/3}$ than when $C_n^2 < 10^{-14}\,\mathrm{m}^{-2/3}$. Furthermore, the mean bias error changes sign between the two cases. MBE is positive when $C_n^2 < 10^{-14}\,\mathrm{m}^{-2/3}$—the scintillometer u_* is larger than the eddy-covariance u_* because of some very large scintillometer u_* values. When $C_n^2 \geq 10^{-14}\,\mathrm{m}^{-2/3}$, on the other hand, MBE is negative—the scintillometer u_* tends to be smaller than the eddy-covariance u_*. The root-mean-square error is also about three times larger when $C_n^2 < 10^{-14}\,\mathrm{m}^{-2/3}$ than when $C_n^2 \geq 10^{-14}\,\mathrm{m}^{-2/3}$. Again, these results seem related to the signal-to-noise ratio.

The Thiermann-Grassl, Edson-Fairall, and Budget functions produced similar values of MBE and RMSE for u_* for the two C_n^2 cases: when $C_n^2 < 10^{-14}\,\mathrm{m}^{-2/3}$ and $C_n^2 \geq 10^{-14}\,\mathrm{m}^{-2/3}$. These metrics for the Wyngaard u_* values were better than for these other three functions when $C_n^2 < 10^{-14}\,\mathrm{m}^{-2/3}$ but worse when $C_n^2 \geq 10^{-14}\,\mathrm{m}^{-2/3}$. The Wyngaard functions again had better convergence success than the other three functions, however, and these additional successes may partly explain the poorer metrics, especially when $C_n^2 \geq 10^{-14}\,\mathrm{m}^{-2/3}$.

5.2 *Rapid Forcing Experiment*

During the Rapid Forcing Experiment, only four in over 200 hours of useful measurements had $C_n^2 < 10^{-14}\,\mathrm{m}^{-2/3}$. Hence, in creating Figs. 3 and 4, I do not distinguish between large and small C_n^2; these figures group all the data into single H_s and u_* scatter plots.

The H_s and u_* scatter plots from the Rapid Forcing Experiment (Figs. 3 and 4) have much different character than the comparable plots from SHEBA (Figs. 1 and 2). The first obvious difference is how much larger H_s was over this mid-latitude, terrestrial site than at SHEBA—H_s was up to 350 W m^{-2}. The negative sensible heat fluxes, however, have comparable magnitude to the SHEBA fluxes and similar clustering and bias—at least when compared with the SHEBA fluxes when $C_n^2 \geq 10^{-14}\,\mathrm{m}^{-2/3}$.

The u_* plots are also much different. The u_* values from the Rapid Forcing Experiment show much more scatter (compare Tables 1 and 2) and, curiously, range up to almost 0.9 m s^{-1}, while the SHEBA u_* values barely reach 0.4 m s^{-1}. Andreas (2011) noticed this limit in SHEBA scintillometer scatter plots of u_* and explained it as an effect of blowing snow.

Briefly, the Scintec scintillometer software does quality checking to decide whether the changes in received laser intensity look like turbulence or like non-turbulent disturbances such as insects flying through the beam. If the intensity changes appear to be insect-induced, the software downgrades NOK. Coincidentally, we noticed during our SHEBA operations that the Scintec software interpreted drifting and blowing snow in the laser beam as insects and, through NOK, flagged the data as bad. Because snow on sea ice begins drifting when u_* is approximately 0.30 m s^{-1} (Andreas 2011), we rarely obtained good scintillometer data from SHEBA when the eddy-covariance u_* was above 0.30 m s^{-1} (Fig. 2).

For the positive H_s values in Fig. 3, the Edson-Fairall functions generally provide the largest scintillometer H_s values. Meanwhile, the Thiermann-Grassl functions provide obviously low values. In Fig. 4, the Edson-Fairall functions also provide the largest scintillometer u_* values; but,

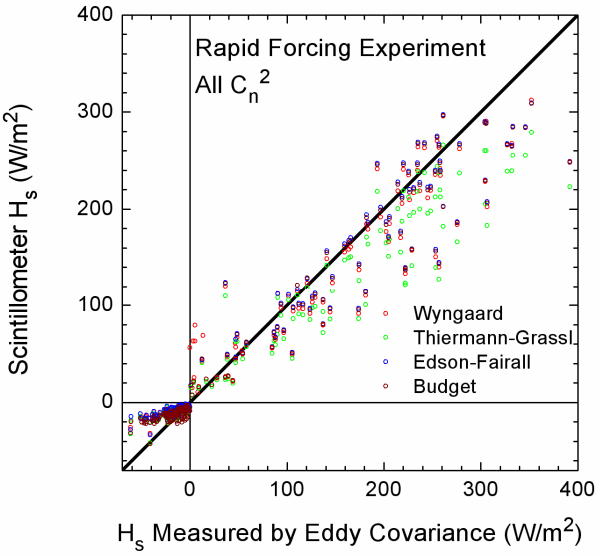

FIG. 3. The hourly scintillometer measurements of sensible heat flux, H_s, from the Rapid Forcing Experiment are compared with simultaneous eddy-covariance measurements of H_s. Four different sets of similarity functions, as described in Section 3.1–3.4, are used for evaluating the scintillometer H_s. The heavy line is 1:1. Since the Rapid Forcing set included only four cases with $C_n^2 < 10^{-14}\,\mathrm{m}^{-2/3}$, this figure shows all the C_n^2 data.

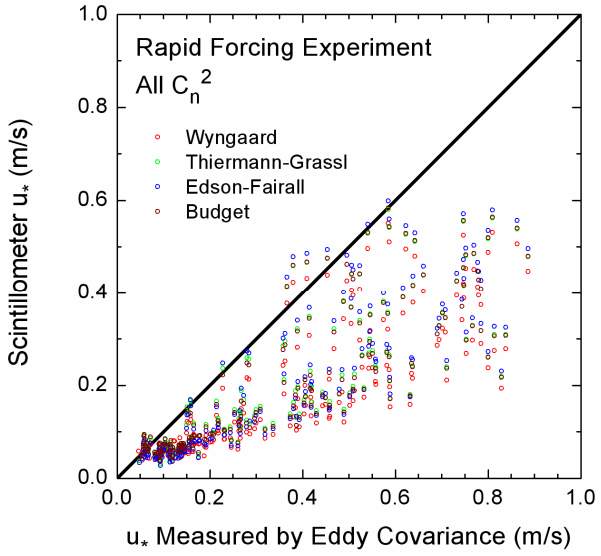

FIG. 4. As in Fig. 3, except this is the scatter plot of friction velocity, u_*.

here, the Wyngaard functions generally give the smallest u_* values. Table 2 reviews the metrics for these two plots.

The correlation coefficients reflected in Figs. 3 and 4 are similar for all four sets of functions (Table 2). The mean bias errors and the root-mean-square errors for the H_s scatter plot, however, are quite varied. The Thiermann-Grassl functions badly underestimate H_s, as we saw during our visual inspection of Fig. 3, and also have the largest RMSE. The MBE for the Budget equations is also about twice as large as for the Wyngaard and Edson-Fairall functions, but the Wyngaard functions lead to more scatter (i.e., a large RMSE).

For the u_* scatter plot (Fig. 4), the Thiermann-Grassl, Edson-Fairall, and Budget functions produce comparable metrics, with the Budget functions yielding slightly poorer fits. The Wyngaard functions produce the most deviant MBE for this plot and the most scatter (largest RMSE).

As in Figs. 1 and 2 and Table 1, however, the Wyngaard functions converged to solutions for H_s and u_* 11–14 times more than did the other three sets of functions for the same input data.

5.3 Consensus u_* Behavior

De Bruin et al. (2002) and Hartogensis et al. (2002) observed similar behavior in a Scintec SLS20 to what we see in Fig. 4 and in the $C_n^2 \geq 10^{-14}\,\mathrm{m}^{-2/3}$ panel in Fig. 2. In their comparisons, too, Scintec scintillometers overestimated u_* for small u_* and underestimated it for large u_* when compared with eddy-covariance measurements. De Bruin et al. speculated that the overestimation at small u_* could result from random noise in the scintillometer and that the underestimation at large u_* might be explained by inactive turbulence, which affects turbulence variances but does no transport and, thus, does not influence fluxes.

TABLE 2. As in Table 1, except these are comparisons for data from the Rapid Forcing Experiment for all ranges of C_n^2.

	Wyngaard	Thiermann-Grassl	Edson-Fairall	Budget
H_s Comparison				
Number	211	200	200	197
Correl. Coef.	0.968	0.972	0.972	0.973
MBE (W m^{-2})	-2.62	-11.52	-2.73	-5.73
RMSE (W m^{-2})	31.26	36.28	29.58	29.60
u_* Comparison				
Number	212	201	201	198
Correl. Coef.	0.838	0.840	0.843	0.835
MBE (m s^{-1})	-0.171	-0.154	-0.153	-0.158
RMSE (m s^{-1})	0.223	0.208	0.204	0.212

Hartogensis et al. (2002) investigated the hypothesis that the separation between transmitted beams in the Scintec SLS20 was not as specified by the manufacturer (and, thus, as used in the processing software), $d = 2.7$ mm. When they recalculated ℓ_0 from their raw Scintec data using $d = 2.6$ mm, the scintillometer-derived u_* agreed better with the eddy-covariance u_* for u_* above 0.2 m s^{-1}; but the scintillometer still overestimated u_* for small u_*.

While it should be possible to incorporate the ideas from De Bruin et al. (2002) into a revised theory of scintillometer behavior, the solution that Hartogensis et al. (2002) tried is not generally practical. If each Scintec scintillometer is built with a slightly different laser beam separation, *d*, these instruments will not be useful off-the-shelf. Each would have to be calibrated against eddy-covariance data to determine *d* before permanent deployment, as Hartogensis et al. have done.

6. SCINTILLOMETER SIMILARITY FUNCTIONS

Although Monin-Obukhov similarity theory is the cornerstone of methods for obtaining surface fluxes from scintillation data, to my knowledge, no one has actually calculated the required similarity functions $g(\zeta)$ and $\phi_\varepsilon(\zeta)$ from scintillometer data. Between the SHEBA and Rapid Forcing datasets, I have enough data to investigate what such scintillometer-derived functions look like.

Here, I will evaluate $g(z/L)$ from (2.6) and $\phi_\varepsilon(z/L)$ from (2.8) by combining the scintillometer measurements of C_n^2 and ε with the corresponding eddy-covariance measurements of u_*, θ_*, and $\zeta = z/L$, where *L* comes from the eddy-covariance measurements according to (2.7). That is, $g(\zeta)$ and $\phi_\varepsilon(\zeta)$ derive from both scintillometer and eddy-covariance measurements, while *L* comes strictly from eddy-covariance measurements.

Figure 5 shows my calculations of $g(z/L)$. The plot also shows the four sets of similarity functions I have been using to derive fluxes: (3.1), (3.3), (3.5), and (3.11). Figure 6 shows $\phi_\varepsilon(z/L)$. This figure has two panels: a large-scale panel that covers the entire z/L range of the data, and a panel that focuses on near-neutral stratification, where the scintillometer-derived ϕ_ε behaves oddly.

Neither set of figures provides any compelling evidence to help us choose among the candidate similarity functions. In fact, from the scatter in these plots, it is not even obvious that the scintillometer data obey Monin-Obukhov similarity. Only for unstable stratification in Fig. 5 [the $g(\zeta)$ plot] do the scintillometer data show any tendency to collapse to a consistent behavior.

Still with regard to Fig. 5, in stable stratification, the scintillometer $g(\zeta)$ values are much smaller for $\zeta > 1$ than suggested by the Wyngaard, Thiermann-Grassl, and Edson-Fairall functions. The Budget $g(\zeta)$ function seems to capture the tendency of the data better here, but the data are so few and scattered that they cannot provide definitive support for this particular Budget function, which relies on the new Grachev et al. (2007) functions, (3.12b) and (3.16b).

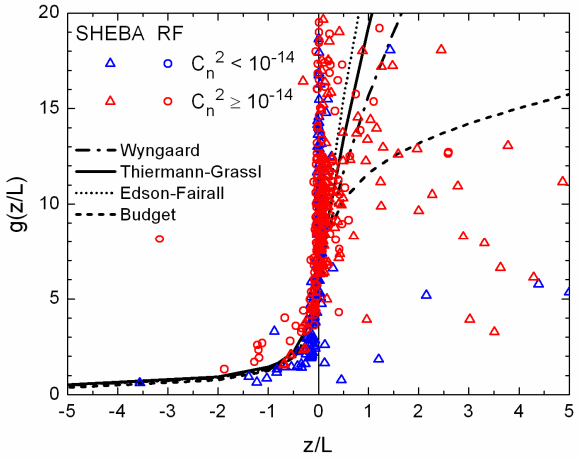

FIG 5. The similarity function $g(z/L)$ is evaluated according to (2.6) from scintillometer measurements of C_n^2 and from eddy-covariance measurements of θ_* and L during SHEBA and the Rapid Forcing Experiment (RF). The data are distinguished by whether $C_n^2 < 10^{-14}\,\mathrm{m}^{-2/3}$ or $C_n^2 \geq 10^{-14}\,\mathrm{m}^{-2/3}$. The four candidate expressions for $g(z/L)$ are also shown: equations (3.1), (3.3), (3.5), and (3.11).

Figure 6 shows $\phi_\varepsilon(\zeta)$ as deduced from both the SHEBA and Rapid Forcing datasets. Again, the data are too scattered to let us choose among the similarity functions. If anything, we can say that, for stable stratification with $\zeta > 1$, the Budget ϕ_ε is the poorest choice among the candidate functions. Again, though, the data offer no evidence that the scintillometer measurements follow Monin-Obukhov similarity.

The right panel in Fig. 6, which focuses on near-neutral stratification, highlights a troubling feature of the scintillometer data and, thus, explains why the Scintec scintillometer generally underestimates u_* (Figs. 2 and 4). The scintillometer-derived ε values produce ϕ_ε values that, on average, are well below one at neutral stratification. Although all of the similarity functions I consider—(3.2), (3.4), (3.6), and (3.15)—predict $\phi_\varepsilon = 1$ for $\zeta = 0$, Fig. 6 suggests that $\phi_\varepsilon \approx 0.3$ for $\zeta = 0$. Figure 6 displays so many small ϕ_ε values because the scintillometer underestimates ε (cf. Hartogensis et al. 2002); as a result, (3.17b) underestimates u_*.

While sporadic suggestions have appeared in the literature that ϕ_ε at neutral stratification does not equal one because production does not perfectly balance dissipation, the imbalance is typically only about 15%: that is, $\phi_\varepsilon \approx 0.85$ near $\zeta = 0$ (e.g., Frenzen and Vogel 1992, 2001). No reliable measurements with traditional turbulence instruments have ever reported $\phi_\varepsilon \sim 0.3$ at neutral stratification. Moreover, both the SHEBA and Rapid Forcing data agree that ϕ_ε is much smaller than one near neutral stratification. In other words, this result cannot be caused by the non-ideal geography of the Rapid Forcing site.

7. CONCLUSIONS

Simultaneous scintillometer and eddy-covariance data from two diverse sites provide a generally consistent picture of how well the Scintec surface-layer scintillometer system SLS20 does in providing path-averaged values of the surface sensible heat flux (H_s) and momentum flux (represented here as the friction velocity, u_*). One site, over Arctic sea ice (the SHEBA experiment), was ideal for micrometeorological research but featured small values of H_s. The second site, a mowed, mid-latitude field in spring (the Rapid Forcing Experiment), provided much larger heat and momentum fluxes but was complex.

The SHEBA data were nearly evenly distributed between cases with $C_n^2 < 10^{-14}\,\mathrm{m}^{-2/3}$ and $C_n^2 \geq 10^{-14}\,\mathrm{m}^{-2/3}$. Generally, scatter plots of scintillometer-derived and eddy-covariance measurements of H_s and u_* showed larger mean bias errors (MBE) and root-mean-square errors (RMSE) when $C_n^2 < 10^{-14}\,\mathrm{m}^{-2/3}$ than when $C_n^2 \geq 10^{-14}\,\mathrm{m}^{-2/3}$. I attribute this effect to poorer signal-to-noise ratio when $C_n^2 < 10^{-14}\,\mathrm{m}^{-2/3}$. This dependence on signal strength probably limits the Scintec's utility for inferring fluxes to situations when the surface layer stratification is not near neutral.

During the Rapid Forcing Experiment, almost all C_n^2 values were above $10^{-14}\,\mathrm{m}^{-2/3}$, but the data metrics corroborated what I saw during SHEBA despite the complexity of the Rapid Forcing site. When the eddy-covariance u_* is small (say 0.1 m s^{-1} or less), the scintillometer tends to overestimate u_*. When the eddy-covariance u_* is larger, the scintillometer underestimates u_*. De Bruin et al. (2002) and Hartogensis et al.

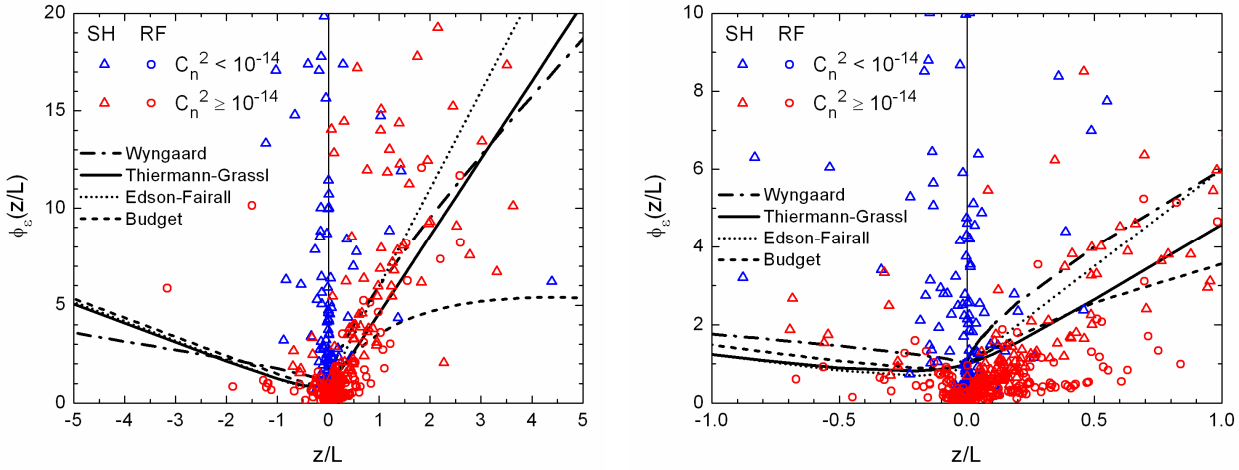

FIG. 6. The similarity function $\phi_\varepsilon(z/L)$ is evaluated according to (2.2) and (2.8) for scintillometer measurements of inner scale, ℓ_0, and from eddy-covariance measurements of u_* and L during SHEBA (SH) and the Rapid Forcing Experiment (RF). The data are distinguished by whether the scintillometer also measured $C_n^2 < 10^{-14}\,\mathrm{m}^{-2/3}$ or $C_n^2 \geq 10^{-14}\,\mathrm{m}^{-2/3}$. The four candidate expressions for $\phi_\varepsilon(z/L)$ are also shown: equations (3.2), (3.4), (3.6), and (3.15). The left panel shows all the data; the right panel focuses on near-neutral stratification.

(2002) observed this same behavior in their Scintec SLS20s.

For the most reliable data—that is, when $C_n^2 \geq 10^{-14}\,\mathrm{m}^{-2/3}$—the scintillometer tended to underestimate the magnitude of the H_s compared to the eddy-covariance value. That is, in stable stratification, when H_s is negative, the scintillometer estimate of H_s was larger (less negative) than the eddy-covariance measurement. In unstable stratification, when H_s was positive, the scintillometer estimate of H_s was smaller (less positive) than the eddy-covariance measurement. This result is explained, at least in part, by the scintillometer's tendency to underestimate u_* because the scintillometer H_s is calculated as $-\rho\, c_p\, u_*\, \theta_*$.

I used four distinct sets of similarity functions, $g(\zeta)$ and $\phi_\varepsilon(\zeta)$, for inferring u_* and H_s from the scintillometer measurements of C_n^2 and ε: designated the Wyngaard, Thiermann-Grassl, Edson-Fairall, and Budget functions. No single set of functions stood out as producing better agreement between scintillometer and eddy-covariance fluxes than the other functions did. The correlation coefficient, the mean bias error, and the root-mean-square error that I used as quality metrics for scatter plots of u_* and H_s were generally similar for the four sets of functions. The Wyngaard functions did converge to solutions more often than the other three functions; but the resulting scintillometer heat fluxes, especially, were usually anomalous.

Alternatively, I used the scintillometer C_n^2 and ε data, in combination with the eddy-covariance measurements of u_*, θ_*, and L, to calculate the similarity functions $g(z/L)$ and $\phi_\varepsilon(z/L)$. This, I believe, is the first time scintillometer data have been used for determining Monin-Obukhov similarity functions. Unfortunately, these calculations also failed to provide any clearer guidance for choosing among the four candidate sets of similarity functions than did the flux comparisons.

Only for a scant sample of data in unstable stratification did the $g(\zeta)$ data show any tendency to collapse to a common curve, as predicted by similarity theory. Otherwise, the $g(\zeta)$ and $\phi_\varepsilon(\zeta)$ data showed no collapse to "universal" similarity functions. As for the question of choosing among the similarity functions, the only conclusions I could make were that the Budget function for $g(\zeta)$ had more appropriate values when $\zeta > 1$ than did the other three functions but that the Budget function for $\phi_\varepsilon(\zeta)$ is too small when $\zeta > 1$.

An important result from these calculations is that the scintillometer data give ϕ_ε estimates at neutral stratification that are near 0.3 instead of the common result $\phi_\varepsilon(\zeta = 0) = 1$. The reason is that the Scintec scintillometer underestimated ε during both the SHEBA and Rapid Forcing experiments. This underestimate of ε is the fundamental reason why the scintillometer-derived u_* was biased low when compared to the eddy-covariance u_* when $u_* > 0.1$ m s^{-1}.

The lack of any consistent behavior in the scintillometer-derived $g(\zeta)$ and $\phi_\varepsilon(\zeta)$ values and this serious underestimate of ϕ_ε at neutral stratification make it impossible for me to conclude that my Scintec scintillometer data follow Monin-Obukhov similarity theory, at least as it is commonly practiced. Although other experiments with other types of scintillometers have indirectly confirmed that Monin-Obukhov similarity works for scintillometer data by producing favorable comparisons between scintillometer and eddy-covariance fluxes (most often, the sensible heat flux), my results urgently recommend direct validation that scintillometers satisfy similarity theory. That is, we need to test whether $g(\zeta)$ and $\phi_\varepsilon(\zeta)$ functions calculated from scintillometer data collapse to universal functions, as I have tried in Figs. 5 and 6. Only when we verify this universal behavior can we confidently use scintillometers for estimating path-averaged fluxes.

8. ACKNOWLEDGMENTS

I would first like to thank Oscar Hartogensis for inviting me to be a keynote speaker at the 3rd Scintillometer Workshop in Wageningen, The Netherlands; his invitation was my impetus to revisit these data. I thank my colleagues in the SHEBA Atmospheric Surface Flux Group for help collecting, processing, and understanding the SHEBA data: Chris Fairall, Andrey Grachev, Peter Guest, Tom Horst, Rachel Jordan, and Ola Persson. I also thank my colleagues in the Rapid Forcing Experiment for help collecting and processing that data: Kerry Claffey, Cathy Geiger, and George Treviño. The U.S. National Science Foundation (NSF) supported this research with award 10-19322. NSF also supported my research during SHEBA with previous awards. The U.S. Department of the Army supported the Rapid Forcing Experiment through Project 61102AT24 at the U.S. Army Cold Regions Research and Engineering Laboratory.

9. REFERENCES

Andreas, E. L, 1987: On the Kolmogorov constants for the temperature-humidity cospectrum and the refractive index spectrum. *J. Atmos. Sci.*, **44,** 2399–2406.

____, 1988: Estimating C_n^2 over snow and sea ice from meteorological data. *J. Opt. Soc. Amer. A*, **5,** 481–495.

____, 1989: Two-wavelength method of measuring path-averaged turbulent surface heat fluxes. *J. Atmos. Oceanic Technol.*, **6,** 280–292.

____, Ed., 1990: *Selected Papers on Turbulence in a Refractive Medium*. SPIE Milestone Series, vol. 25, Society of Photo-Optical Instrumentation Engineers, Bellingham, WA, 693 pp.

____, 1992: Uncertainty in a path-averaged measurement of the friction velocity u_*. *J. Appl. Meteor.*, **31,** 1312–1321.

____, 2011: The fallacy of drifting snow. *Bound.-Layer Meteor.*, **141,** 333–347.

____, C. W. Fairall, P. S. Guest, and P. O. G. Persson, 1999: An overview of the SHEBA atmospheric surface flux program. *Fifth Conf. on Polar Meteorology and Oceanography*, Dallas, TX, Amer. Meteor. Soc., 411–416.

____, ____, P. O. G. Persson, and P. S. Guest, 2003: Probability distributions for the inner scale and the refractive index structure parameter and their implications for flux averaging. *J. Appl. Meteor.*, **42,** 1316–1329.

____, K. J. Claffey, R. E. Jordan, C. W. Fairall, P. S. Guest, P. O. G. Persson, and A. A. Grachev, 2006a: Evaluations of the von Kármán constant in the atmospheric surface layer. *J. Fluid Mech.*, **559,** 117–149.

____, C. A. Geiger, K. J. Claffey, G. Treviño, and C. C. Ryerson, 2006b: Rapid forcing of the surface and near-surface atmosphere. *10th Symp. on Integrated Observing and Assimilation Systems for the Atmosphere, Oceans, and Land Surface*, Atlanta, GA, Amer. Meteor. Soc., CD-ROM 4.2, 12 pp.

____, ____, G. Treviño, and K. J. Claffey, 2008a: Identifying nonstationarity in turbulence series. *Bound.-Layer Meteor.*, **127,** 37–56.

____, P. O. G. Persson, and J. E. Hare, 2008b: A bulk turbulent air-sea flux algorithm for high-wind, spray conditions. *J. Phys. Oceanogr.*, **38,** 1581–1596.

____, T. W. Horst, A. A. Grachev, P. O. G. Persson, C. W. Fairall, P. S. Guest, and R. E. Jordan, 2010a: Parametrizing turbulent exchange over summer sea ice and the marginal ice zone. *Quart. J. Roy. Meteor. Soc.*, **136,** 927–943.

____, P. O. G. Persson, R. E. Jordan, T. W. Horst, P. S. Guest, A. A. Grachev, and C. W. Fairall, 2010b: Parameterizing turbulent exchange over sea ice in winter. *J. Hydrometeor.*, **11,** 87–104.

Beyrich, F., H. A. R. De Bruin, W. M. L. Meijninger, J. W. Schipper, and H. Lohse, 2002: Results from one-year continuous operation of a large aperture scintillometer over a heterogeneous land surface. *Bound.-Layer Meteor.*, **105,** 85–97.

Chehbouni, A., and 10 coauthors, 1999: Estimation of area-average sensible heat flux using a large-aperture scintillometer during the Semi-Arid Land-Surface-Atmosphere (SALSA) Experiment. *Water Resour. Res.*, **35,** 2505–2511.

Coulter, R. L., and M. L. Wesley, 1980: Estimates of surface heat flux from sodar and laser scintillation measurements in the unstable boundary layer. *J. Appl. Meteor.*, **19,** 1209–1222.

Davidson, K. L., T. M. Houlihan, C. W. Fairall, and G. E. Schacher, 1978: Observation of the temperature structure function parameter, C_T^2, over the ocean. *Bound.-Layer Meteor.*, **15,** 507–523.

De Bruin, H. A. R., B. J. J. M. Van den Hurk, and W. Kohsiek, 1995: The scintillation method tested over a dry vineyard area. *Bound.-Layer Meteor.*, **76,** 25–40.

____, W. M. L. Meijninger, A.-S. Smedman, and M. Magnusson, 2002: Displaced-beam small aperture scintillometer test. Part I: The WINTEX data-set. *Bound.-Layer Meteor.*, **105,** 129–148.

Edson, J. B., and C. W. Fairall, 1998: Similarity relationships in the marine atmospheric surface layer for terms in the TKE and scalar variance budgets. *J. Atmos. Sci.*, **55,** 2311–2328.

Fairall, C. W., and S. E. Larsen, 1986: Inertial-dissipation methods and turbulent fluxes at the air-ocean interface. *Bound.-Layer Meteor.*, **34,** 287–301.

____, G. E. Schacher, and K. L. Davidson, 1980: Measurements of the humidity structure function parameters, C_q^2 and C_{Tq}, over the ocean. *Bound.-Layer Meteor.*, **19,** 81–92.

Frenzen, P., and C. A. Vogel, 1992: The turbulent kinetic energy budget in the atmospheric surface layer: A review and an experimental reexamination in the field. *Bound.-Layer Meteor.*, **60,** 49–76.

____, and ____, 2001: Further studies of atmospheric turbulence in layers near the surface: Scaling the TKE budget above the roughness sublayer. *Bound.-Layer Meteor.*, **99,** 173–206.

Grachev, A. A., C. W. Fairall, P. O. G. Persson, E. L Andreas, and P. S. Guest, 2005: Stable boundary-layer scaling regimes: The SHEBA data. *Bound.-Layer Meteor.*, **116,** 201–235.

____, E. L Andreas, C. W. Fairall, P. S. Guest, and P. O. G. Persson, 2007: SHEBA flux-profile relationships in the stable atmospheric boundary layer. *Bound.-Layer Meteor.*, **124,** 315–333.

Green, A. E., K. J. McAneney, and M. S. Astill, 1994: Surface-layer scintillation measurements of daytime sensible heat and momentum fluxes. *Bound.-Layer Meteor.*, **68,** 357–373.

____, ____, and J. P. Lagouarde, 1997: Sensible heat and momentum flux measurement with an optical inner scale meter. *Agricult. Forest Meteor.*, **85,** 259–267.

Hartogensis, O. K., H. A. R. De Bruin, and B. J. H. Van de Wiel, 2002: Displaced-beam small aperture scintillometer test. Part II: CASES-99 stable boundary-layer experiment. *Bound.-Layer Meteor.*, **105,** 149–176.

Hill, R. J., 1978: Spectra of fluctuations in refractivity, temperature, humidity, and temperature-humidity cospectrum in the inertial and dissipation ranges. *Radio Sci.*, **13,** 953–961.

____, 1989: Implications of Monin-Obukhov similarity theory for scalar quantities. *J. Atmos. Sci.*, **46,** 2236–2244.

____, 1997: Algorithms for obtaining atmospheric surface-layer fluxes from scintillation measurements. *J. Atmos. Oceanic Technol.*, **14,** 456–467.

____, and S. F. Clifford, 1978: Modified spectrum of atmospheric temperature fluctuations and its application to optical propagation. *J. Opt. Soc. Amer.*, **68,** 892–899.

____, G. R. Ochs, and J. J. Wilson, 1992: Measuring surface-layer fluxes of heat and

momentum using optical scintillation. *Bound.-Layer Meteor.*, **58,** 391–408.

Kaimal, J. C., and J. J. Finnigan, 1994: *Atmospheric Boundary Layer Flows: Their Structure and Measurement*. Oxford University Press, 289 pp.

____, and J. E. Gaynor, 1991: Another look at sonic thermometry. *Bound.-Layer Meteor.*, **56,** 401–410.

____, ____, H. A. Zimmerman, and G. A. Zimmerman, 1990: Minimizing flow distortion errors in a sonic anemometer. *Bound.-Layer Meteor.*, **53,** 103–115.

Kleissl, J., J. Gomez, S.-H. Hong, J. M. H. Hendrickx, T. Rahn, and W. L. Defoor, 2008: Large aperture scintillometer intercomparison study. *Bound.-Layer Meteor.*, **128,** 133–150.

Kohsiek, W., 1982: Measuring C_T^2, C_Q^2, and C_{TQ} in the unstable surface layer, and relations to the vertical fluxes of heat and moisture. *Bound.-Layer Meteor.*, **24,** 89–107.

Large, W. G., and S. Pond, 1981: Open ocean momentum flux measurements in moderate to strong winds. *J. Phys. Oceanogr.*, **11,** 324–336.

____, and ____, 1982: Sensible and latent heat flux measurements over the ocean. *J. Phys. Oceanogr.*, **12,** 464–482.

Panofsky, H. A., and J. A. Dutton, 1984: *Atmospheric Turbulence: Models and Methods for Engineering Applications.* John Wiley and Sons, 397 pp.

Paulson, C. A., 1970: The mathematical representation of wind speed and temperature profiles in the unstable atmospheric surface layer. *J. Appl. Meteor.*, **9,** 857–861.

Persson, P. O. G., C. W. Fairall, E. L Andreas, P. S. Guest, and D. K. Perovich, 2002: Measurements near the Atmospheric Surface Flux Group tower at SHEBA: Near-surface conditions and surface energy budget. *J. Geophys. Res.*, **107,** (C10) 8045, doi:10.1029/2000JC000705.

Sreenivasan, K. R., 1996: The passive scalar spectrum and the Obukhov-Corrsin constant. *Phys. Fluids*, **8,** 189–196.

Taylor, R. J., 1961: A new approach to the measurement of turbulent fluxes in the lower atmosphere. *J. Fluid Mech.*, **10,** 449–458.

Thiermann, V., 1992: A displaced-beam scintillometer for line-averaged measurements of surface layer turbulence. *Tenth Symp. on Turbulence and Diffusion*, Portland, OR, Amer. Meteor. Soc., 244–247.

____, and H. Grassl, 1992: The measurement of turbulent surface-layer fluxes by use of bichromatic scintillation. *Bound.-Layer Meteor.*, **58,** 367–389.

Uttal, T., and 27 coauthors, 2002: Surface Heat Budget of the Arctic Ocean. *Bull. Amer. Meteor. Soc.*, **83,** 255–275.

Wesley, M. L., 1976: A comparison of two optical methods for measuring line averages of thermal exchanges above warm water surfaces. *J. Appl. Meteor.*, **15,** 1177–1188.

Willmott, C. J., 1982: Some comments on the evaluation of model performance. *Bull. Amer. Meteor. Soc.*, **63,** 1309–1313.

Wyngaard, J. C., 1973: On surface-layer turbulence. *Workshop on Micrometeorology*, D. A. Haugen, Ed., American Meteorological Society, 101–149.

____, 2010: *Turbulence in the Atmosphere*. Cambridge University Press, 393 pp.

____, and S. F. Clifford, 1978: Estimating momentum, heat and moisture fluxes from structure parameters. *J. Atmos. Sci.*, **35,** 1204–1211.

____, and O. R. Coté, 1971: The budgets of turbulent kinetic energy and temperature variance in the atmospheric surface layer. *J. Atmos. Sci.*, **28,** 190–201.

____, Y. Izumi, and S. A. Collins, Jr., 1971: Behavior of the refractive-index-structure parameter near the ground. *J. Opt. Soc. Amer.*, **61,** 1646–1650.